



OPEN

Coating the surface of interconnected Cu₂O nanowire arrays with HKUST-1 nanocrystals via electrochemical oxidation

Francesco Caddeo^{1,2,5}, Florian Himmelstein^{1,2}, Behzad Mahmoudi^{1,2}, Ana María Araújo-Cordero^{1,2}, Denis Eberhart^{1,2}, Haojie Zhang^{1,3,6}, Titus Lindenberg^{1,2}, Angelika Hähnel⁴, Christian Hagendorf⁴ & A. Wouter Maijenburg^{1,2}✉

Controlling the crystallization of Metal–Organic Frameworks (MOFs) at the nanoscale is currently challenging, and this hinders their utilization for multiple applications including photo(electro) chemistry and sensors. In this work, we show a synthetic protocol that enables the preparation of highly homogeneous Cu₂O@MOF nanowires standing on a conductive support with extensive control over the crystallization of the MOF nanoparticles at the surface of the Cu₂O nanowires. Cu₂O nanowires were first prepared via templated electrodeposition, and then partially converted into the well-known Cu-MOF HKUST-1 by pulsed electrochemical oxidation. We show that the use of PVP as a capping agent during the electrochemical oxidation of Cu₂O into HKUST-1 provides control over the growth of the MOF nanocrystals on the surface of the Cu₂O nanowires, and that the size of the MOF crystals obtained can be tuned by changing the concentration of PVP dissolved in the electrolyte. In addition, we propose the use of benzoic acid as an alternative to achieve control over the size of the obtained MOF nanocrystals when the use of a capping agent should be avoided.

Metal–Organic Frameworks (MOFs) are a class of crystalline nanoporous materials that hold high promises for a wide range of applications, including gas storage¹, gas separation², sensors³, drug delivery⁴ and heterogeneous (photo)catalysis^{5–7}. In recent years, increasing efforts have been devoted in the MOF community towards the development of synthetic methods that enable tuning the MOF crystal growth at the nanoscale regime⁸, i.e. the so-called nano-MOFs, which include microwave⁹, sonochemical¹⁰, solvothermal¹¹, microemulsion¹² and droplet-based microfluidic synthesis¹³. The size control of MOF crystals at the nanoscale is particularly important in the field of heterogeneous catalysis, where the diffusion of reactive species through the MOF's nanoporous architecture plays a very important role in terms of efficiency¹⁴.

Another class of synthetic methods that is considered highly promising in view of processability and large-scale preparation of MOFs is electrochemical synthesis^{15–17}. Among all different electrochemical methods, including anodic oxidation¹⁸, reductive deprotonation¹⁹, galvanic replacement²⁰ and electrophoretic deposition²¹, the anodic oxidation of a metallic substrate immersed in an electrolyte containing the appropriate organic linker is the most widely used, since it has several advantages including mild synthetic conditions, nontoxic solvents and short reaction times. Many well-known MOFs have been synthesized via anodic oxidation so far, including HKUST-1²², ZIF-8²³, MIL-100²⁴, MOF-5²⁵ and UiO-66²⁶.

In addition to metallic substrates, metal oxides could also be used as starting materials for the preparation of MOFs through anodic oxidation, provided that the metal cations can undergo further oxidation. For example, Cu⁺ ions in Cu₂O can be further oxidized to Cu²⁺, favoring the formation of Cu-based MOFs. To the best of our knowledge, the electrochemical synthesis of Cu-based MOFs through the direct anodic oxidation of Cu₂O

¹Center for Innovation Competence SiLi-Nano, Martin Luther University Halle-Wittenberg, Karl-Freiherr-von-Fritsch-Straße 3, 06120 Halle (Saale), Germany. ²Institute of Chemistry, Martin Luther University Halle-Wittenberg, Kurt-Mothes-Straße 2, 06120 Halle (Saale), Germany. ³Institute of Physics, Martin Luther University Halle-Wittenberg, Heinrich-Damerow-Straße 4, 06120 Halle (Saale), Germany. ⁴Fraunhofer Center for Silicon Photovoltaics CSP, Otto-Eißfeldt-Straße 12, 06120 Halle (Saale), Germany. ⁵Present address: Center for Hybrid Nanostructures (CHyN), Institute of Nanostructure and Solid State Physics, University of Hamburg, 22607 Hamburg, Germany. ⁶Present address: Max Planck Institute of Microstructure Physics, Weinberg 2, 06120 Halle (Saale), Germany. ✉email: wouter.maijenburg@chemie.uni-halle.de

has not been studied yet. However, it has been shown first by Schäfer et al.²⁷ and then confirmed by our recent work²⁸ that Cu₂O is formed as an intermediate during the electrochemical conversion of metallic Cu into the MOF HKUST-1, and therefore we propose here that Cu₂O could also be directly used as a starting material for the electrochemical preparation of Cu-based MOFs. Additionally, HKUST-1 was also prepared using techniques such as chemical-vapor deposition (CVD), solvothermal or sol-gel synthesis through the conversion of Cu-based precursors including Cu or CuO films and Cu(II) hydroxide^{29–31}.

Cu₂O nanostructures have been proposed as promising candidates for a number of applications, including photovoltaics³², photoelectrochemical water splitting³³, lithium-ion batteries³⁴, sensors³⁵ and catalysis³⁶. Cu₂O nanowires in particular have received attention in the field of photoelectrochemical (PEC) water splitting³⁷, since their shape allows efficient light absorption over their length, whereas the minority charge carriers can be collected across their diameter, effectively overcoming the problems related to the well-known mismatch between the light absorption depth and minority charge carrier diffusion length of this material^{38,39}.

An easy and inexpensive way to obtain metal oxide nanowires is by templated electrodeposition within the pores of ion-track etched polycarbonate membranes. These commercially available membranes are fabricated by swift heavy ion irradiation and subsequent chemical etching, and can be obtained with tuneable pore diameters (from 20 nm to several micrometers), pore densities (1 to 10¹⁰ pores·cm⁻²) and different pore arrangements (from parallel arrays to highly interconnected pores)^{40–42}. The highly interconnected arrangement in particular gives the possibility to obtain nanowires with a high aspect ratio (length/diameter up to 1000) due to the increased mechanical stability, with the length of the nanowires being tuned by the electrodeposition time^{43,44}. Cu₂O nanowires obtained via this technique were recently investigated as photocathodes for PEC water splitting⁴⁵.

In our recent work, we introduced a synthetic protocol that combined the templated electrodeposition of Cu nanowires within the pores of ion-track etched membranes and their conversion into HKUST-1 nanowires via anodic oxidation²⁸. In that work, Cu nanowires were electrochemically converted into MOFs while being enclosed within the polycarbonate membrane used as a template, therefore generating MOF nanowires with tuned diameters, since the crystallization of the MOF was constrained within the pores of the membrane.

In addition to the formation of nanowires that fully consist of HKUST-1, another interesting avenue is the preparation of MOF coatings on various nanostructures, therefore generating hybrid materials with synergistic properties. For example, Huang et al.⁴⁶ developed a general strategy for the synthesis of ZIF-8 coatings via surface modification on various substrates, including carbon nanotubes (CNTs), SiO₂, NiO and Fe₂O₃ nanostructures; Hu et al.⁴⁷ showed the epitaxial growth of a 2D MOF on a pristine graphene surface for electrochemical applications; He et al.⁴⁸ reported a ternary TiO₂-Cu₂O-HKUST-1 composite material synthesized through the in-situ growth of HKUST-1 on the TiO₂-Cu₂O surface, making use of part of the Cu₂O as sacrificial copper source, which was tested for the photocatalytic reduction of CO₂ to CH₄; Zhan et al.⁴⁹ prepared ZnO@ZIF-8 nanowires and tested their performance as a sensor for the detection of H₂O₂; Demirel et al.⁵⁰ studied the electrochemical synthesis of HKUST-1 coatings on hollow copper fibers via anodic dissolution; Wu et al.⁵¹ prepared cubic Cu₂O@HKUST-1 nanostructures via an in-situ conversion procedure and tested the material for the photocatalytic degradation of tetracycline hydrochloride. In addition to these examples, many more important papers and reviews have been published on this subject^{17,52–56}.

In this work, we combined templated electrodeposition in polycarbonate membranes with subsequent anodic dissolution to prepare interconnected core-shell Cu₂O@HKUST-1 nanowires standing on a conductive substrate. In addition, we studied the influence of PVP and benzoic acid as additives in the electrolyte used for the anodic dissolution to control the crystal growth of the obtained HKUST-1 nanoparticles at the surface of the Cu₂O nanowires.

Results and discussion

Standing Cu₂O nanowires via templated electrodeposition inside polycarbonate membranes.

Cu₂O nanowires standing on a conductive substrate were prepared by templated electrodeposition using commercially available polycarbonate membranes as the template. In Fig. 1a–d, a schematic representation of the process is shown, while photographs of the samples for each synthetic step are reported in Fig. S1, and SEM images of the bare polycarbonate membranes are reported in Fig. S2. As a first step, 200 nm of Au and 500 nm of Cu were consecutively deposited on one side of the polycarbonate membrane via sputtering (Fig. 1b and S1a,b). This sputtering step has a dual function: making one side of the membrane conductive and at the same time closing the pores of the membrane. Cu was chosen as a cheap and earth-abundant material for the back side of our electrodes, whereas Au was used as an intermediate layer for its good adhesion to the polycarbonate membrane. After sputtering, a thick layer (hundreds of micrometers) of metallic Cu was deposited on the conductive side of the membrane using a previously reported electrodeposition recipe⁴³ (Fig. S1c) in order to obtain a mechanically stable electrode.

Once the back side of the electrode was ready, p-Cu₂O was electrodeposited inside the pores of the membrane (Fig. 1c) following a previously reported procedure^{45,57,58}, obtaining Cu₂O nanowires. Here, the choice of the polycarbonate membrane determines the diameter of the nanowires, the nanowire density and their organization, and the electrodeposition time determines the nanowire length. For this study, we chose polycarbonate membranes with a pore diameter of 200 nm and a pore density of 5·10⁸ cm⁻². Moreover, the membranes used have interconnected pores, which in turn generate interconnected nanowires as shown in Fig. 1c, k, i. For all of the samples presented in this study, we used an electrodeposition time of 2000s (~33 min), which generated nanowires with a length of ca. 10 μm, corresponding to an aspect ratio of 50. In this respect, it should be mentioned that previous works have been published on vertically grown one-dimensional arrays of nanowires, including the work by the Grätzel group on Cu₂O nanowires³⁷. However, such vertically aligned non-interconnected nanowires can be prepared only with a rather limited aspect ratio due to their intrinsic fragility. Therefore, in this work, we

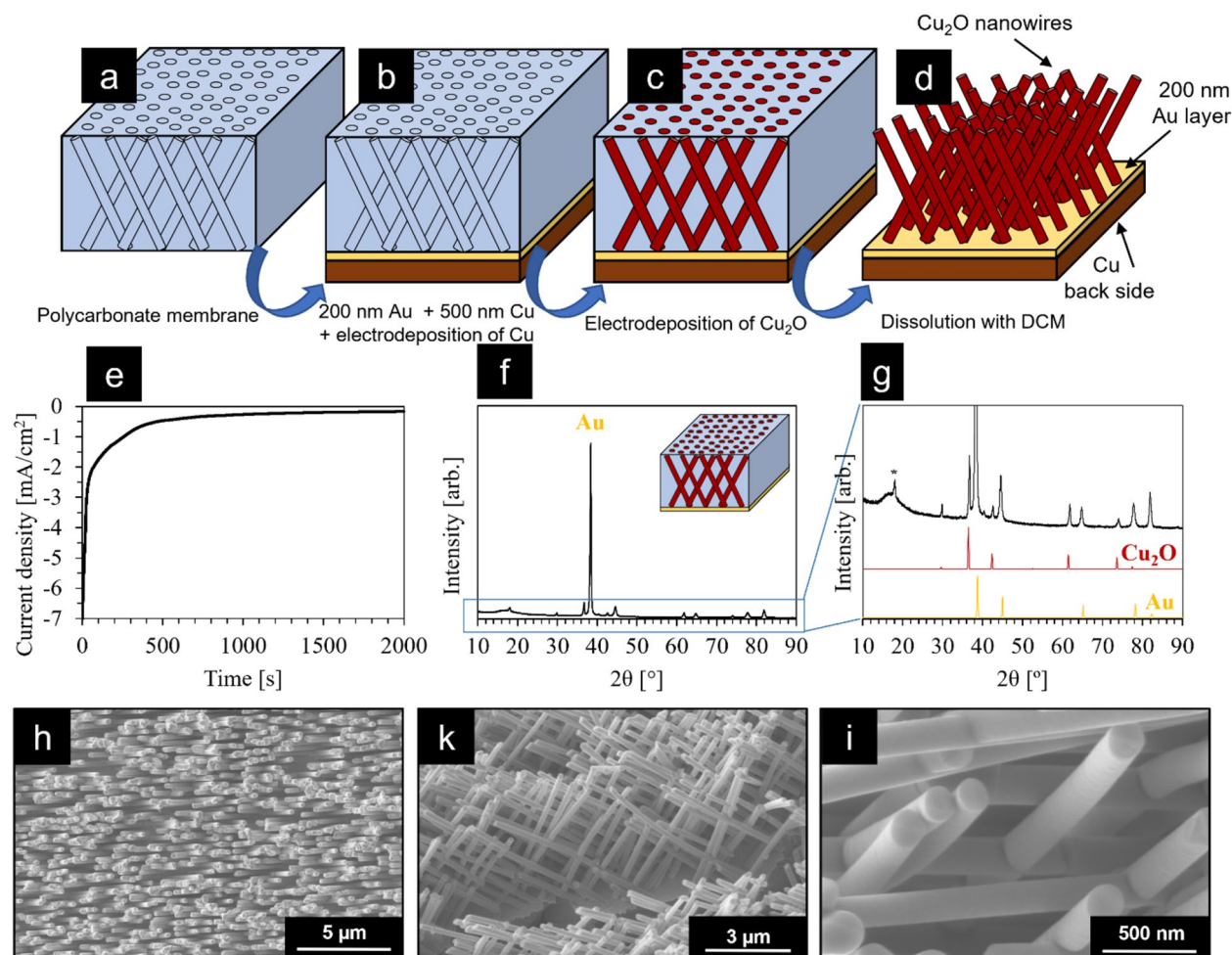


Figure 1. Preparation of interconnected Cu_2O nanowire arrays. (a–d) Schematic representation of the synthetic steps used for the preparation of the Cu_2O nanowires: (a) polycarbonate membrane; (b) sputtering of Au and Cu on one side of the membrane and electrodeposition of Cu on the same side; (c) electrodeposition of Cu_2O inside the pores of the membrane; (d) dissolution of the membrane to obtain standing Cu_2O nanowires; (e) chronoamperogram obtained during the electrodeposition of the Cu_2O nanowires at -0.4 V versus a Cu counter electrode; (f) XRD pattern of the Cu_2O nanowires (Au reference card: ICSD code: 44,362; Cu_2O reference card: ICSD code: 180,846) (with the inset showing a representation of the sample measured, i.e. Cu_2O nanowires within the polycarbonate membrane, with only a 200 nm gold layer on the back side of the membrane); (g) enlarged area of the XRD pattern in (f); (h) top-view SEM image of the Cu_2O nanowires; (k) side-view SEM image of the nanowires; (i) high-magnification SEM image of the same nanowires.

also highlight the importance of using templates with interconnected pores in order to obtain interconnected nanowire arrays with enhanced mechanical stability, allowing to obtain higher aspect ratios.

Once the electrodeposition was successfully carried out, the polycarbonate membranes were dissolved with dichloromethane (DCM), yielding standing Cu_2O nanowires (Fig. 1d). A photograph of a sample after the dissolution step with DCM is given in Fig. S1d. Figure 1e shows a typical chronoamperogram that was recorded during the electrodeposition of the p- Cu_2O nanowires within the pores of the membrane. At the first stage, the deposition proceeds at high current densities since the conductive Au back electrode allows a fast deposition. After ~ 300 s, the current density decreases considerably due to the deposition happening on top of the already deposited semiconducting Cu_2O nanowires, reaching a steady-state current density of ca. $200 \mu\text{A cm}^{-2}$.

The XRD pattern in Fig. 1f,g refers to the electrodeposited Cu_2O nanowires inside a membrane with only sputtered Au as the back contact and without the additional Cu deposited on the back side, as shown in the inset in Fig. 1f. The XRD pattern therefore shows Cu_2O reflections that can only originate from the electrodeposition inside the pores. Apart from a large contribution at $\sim 16^\circ$ coming from the amorphous polycarbonate (Fig. S3) and the peak indicated with an asterisk that originates from the Teflon tape used to fix the sample onto the XRD sample holder (Fig. S4), all other XRD reflections could be assigned to either Au or Cu_2O ^{59,60}.

Figure 1h,i show SEM images of the as-prepared Cu_2O nanowires after dissolution of the polycarbonate membrane in DCM. The low-magnification SEM image in Fig. 1h shows that the samples are highly homogeneous with the nanowires growing within all pores of the membrane. Figure 1k shows a side-view SEM image of

the nanowires and Fig. 1i is a high-magnification SEM image that clearly shows the very smooth surface of the Cu₂O nanowires, indicating the high crystallinity of the deposited nanowires.

Partial conversion of Cu₂O into HKUST-1. In the next step, the Cu₂O nanowires were partially converted into the well-known Cu-based MOF HKUST-1 (Cu₃(BTC)₂; BTC = 1,3,5-benzenetricarboxylic acid), with the aim to obtain Cu₂O nanowires decorated with MOF nanoparticles. This was achieved via electrochemical oxidation of the Cu₂O nanowires and simultaneous formation of HKUST-1, with a special emphasis on the fine-tuning of a number of synthetic parameters, including the electrochemical oxidation process, the presence of appropriate additives in the electrolyte and the reaction time. For the electrochemical oxidation, a 2-electrode setup was used with the Cu₂O nanowires presented in the previous section as the working electrode and a Cu wire as the counter electrode.

First of all, we decided to employ a pulsed electrochemical oxidation process, in which the potential was alternated 100 times between 2.5 and 0.0 V (vs. a Cu counter electrode), which were applied for 0.1 and 0.5 s, respectively. This choice is motivated by our goal to obtain a composite material where Cu₂O nanowires are decorated with MOF nanoparticles in a core-shell type structure. We imagine that while Cu⁺ ions from Cu₂O are oxidized to Cu²⁺ during the pulses at 2.5 V, a certain time is needed for these ions to react with the BTC molecules and to form MOF nanocrystals at the surface of the Cu₂O nanowires. Additionally, in one of our previous studies, we performed the complete electrochemical conversion of Cu nanowires into HKUST-1 using the same electrolyte, but by applying a continuous potential 2.5 V versus Cu for 2 h, and we verified that the obtained HKUST-1 nanowires were stable in these oxidizing conditions²⁸.

Moreover, it should be highlighted that the use of appropriate additives dissolved in the electrolyte, i.e. PVP and benzoic acid, also greatly contributed to the successful formation of MOF nanoparticles at the surface of the Cu₂O nanowires. In fact, when performing the electrochemical conversion of Cu₂O using an ethanolic solution of BTC without any additive, very large HKUST-1 crystals were found that do not adhere to the surface of the Cu₂O nanowires, as shown in the SEM images in Fig. S5. A similar result was obtained in a recent study by Luo et al., during the electrochemical conversion of Cu nanowires into HKUST-1 in the absence of appropriate additives⁶¹. Therefore, in order to control the growth of the MOF crystals during the electrochemical oxidation, we first explored the influence of PVP dissolved in the electrolyte using two different concentrations, i.e. 5 and 1 mg mL⁻¹, and as can be seen in Fig. 2b–d, this resulted in the controlled formation of MOF nanocrystals around the Cu₂O nanowires. Indeed, PVP is a well-known capping agent, which is broadly used in nano-chemistry to control the growth of different kinds of nanoparticles^{62,63}. Moreover, while PVP was rarely used in previous studies during the synthesis of HKUST-1, it must be highlighted that Li et al.⁶⁴ showed the PVP-mediated synthesis of HKUST-1 octahedron nanoparticles with sizes ranging from 50 to 500 nm.

Another important parameter of the conversion process is the overall reaction time. In fact, it is known from previous reports that Cu₂O also converts into Cu₃(BTC)₂ without applying any electrochemical potential, in which dissolved oxygen from the air acts as the oxidizing agent⁵⁴. Therefore, the time that the Cu₂O nanowires were immersed in the electrolyte represents an important parameter, as the conversion reaction also proceeds before and after the pulsed electrochemical process. Here, we show results corresponding to overall reaction times of 10 and 30 min, of which only 1 min was used for the actual electrochemical oxidation, with the oxidative potential of 2.5 V only being applied for 10 s.

Fig. S6 shows a typical chronoamperogram of the process, with an enlarged area of the chronoamperogram being reported in the inset of the figure. A current density of ca. 70 μA cm⁻² was generated during the pulses at the oxidative potential of 2.5 V, corresponding to the oxidation of Cu⁺ into Cu²⁺. Figure 2a shows XRD patterns of the materials obtained using PVP as a capping agent together with the XRD pattern of HKUST-1 calculated from single crystal data⁶⁵. Due to the small size of the obtained HKUST-1 nanoparticles and their presence in a small quantity in terms of overall mass, the reflections from the MOF crystals are very weak compared to the ones associated to Cu₂O, Cu and Au. Therefore, Fig. 2a shows the XRD patterns in the 2θ range of 5–15°, where the most prominent reflections corresponding to HKUST-1 are present, whereas the entire range is shown in Fig. S7. All XRD patterns show the presence of HKUST-1. In the case of the sample obtained using PVP with a concentration of 5 mg mL⁻¹ and a total reaction time of 10 min, only the most intense reflection at 2θ = 11.7° (full width at half maximum (FWHM) = 0.36°, corresponding to a crystallite size of ca. 27 nm calculated with the Debye–Scherrer method) is visible due to the small size and small amount of the MOF nanoparticles (Fig. 2b). With increasing the overall reaction time to 30 min, this reflection becomes more intense, and additionally we can observe the appearance of the second most intense reflection centered at 2θ = 9.6°. These reflections are broad with a FWHM of 0.27° for 2θ = 11.7° and 0.34° for 2θ = 9.6°, corresponding to a crystallite size of ca. 38 nm and 29 nm, respectively, suggesting crystal growth when compared to the sample obtained after 10 min, as also observed in Fig. 2c. The XRD pattern of the material obtained by decreasing the concentration of PVP to 1 mg mL⁻¹ and by keeping an overall reaction time of 30 min shows all the reflections corresponding to HKUST-1 in this 2θ range. Moreover, the peaks appear sharper, with the FWHM of the peak at 2θ = 11.7° being 0.18°, which corresponds to a crystallite size of ca. 64 nm calculated with the Debye–Scherrer method. This enhancement of size of the HKUST-1 nanoparticles is in agreement with the obtained SEM image from this sample (Fig. 2d).

When taking a closer look at the SEM images of the Cu₂O@HKUST-1 nanowires obtained using PVP with a concentration of 5 mg mL⁻¹ after a total reaction time of 10 min (Fig. 2b) and 30 min (Fig. 2c), it can be seen that the Cu₂O nanowires appear discontinuously decorated with the MOF nanoparticles at their surface along the full nanowire length. Increasing the reaction time from 10 to 30 min resulted in larger nanoparticles that appear to cover most of the surface of the Cu₂O nanowires, as shown in Fig. 2c. These evidences agree with the XRD patterns (Fig. 2a) and with the presence of MOF nanoparticles as a result of the electrochemical oxidation of Cu₂O.

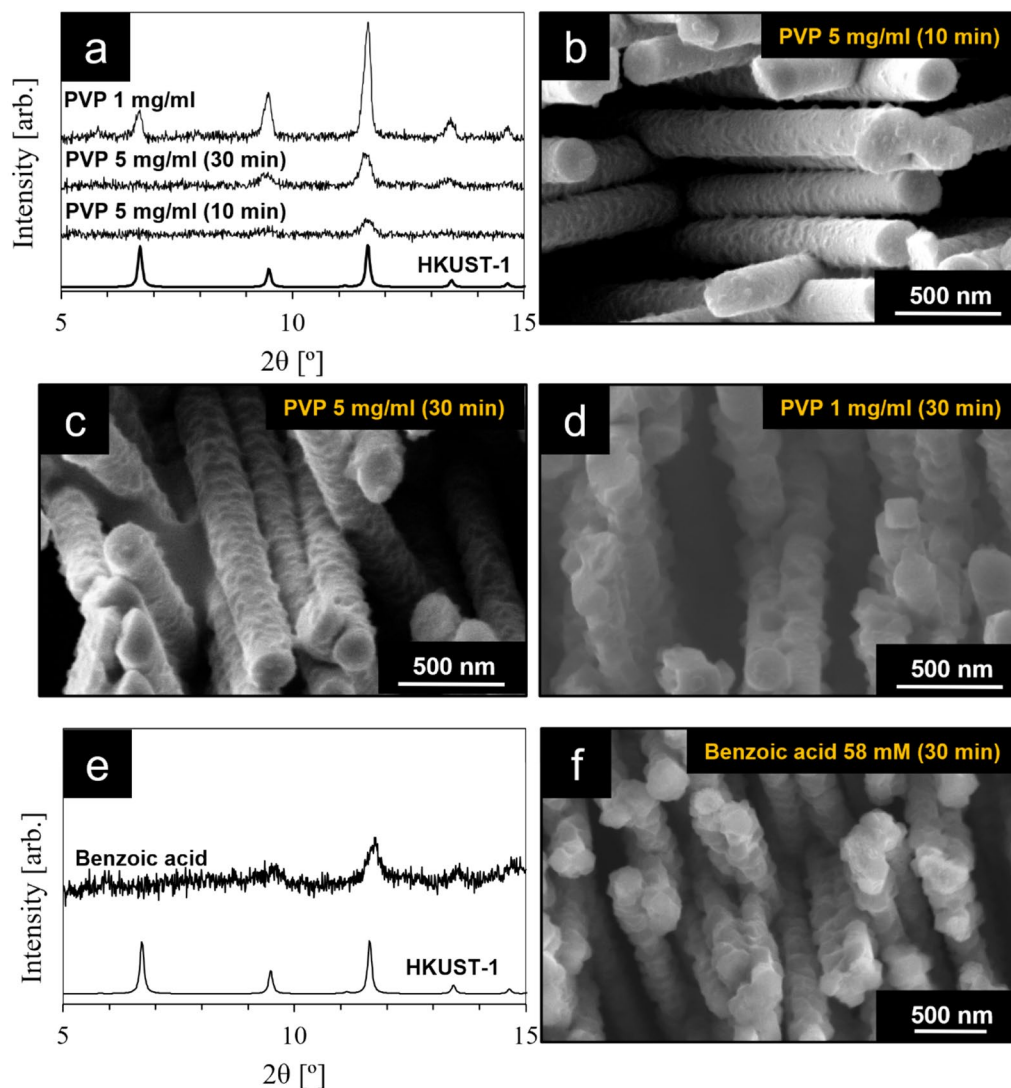


Figure 2. Effect of additives and reaction time on the partial conversion of Cu_2O into HKUST-1. (a) XRD patterns of the nanowires after partial conversion of Cu_2O into HKUST-1 in the presence of PVP as a capping agent; (b) SEM image of the $\text{Cu}_2\text{O}@$ HKUST-1 nanowires obtained with a PVP concentration of 5 mg mL^{-1} and an overall reaction time of 10 min; (c) SEM image of $\text{Cu}_2\text{O}@$ HKUST-1 nanowires obtained with a PVP concentration of 5 mg mL^{-1} and an overall reaction time of 30 min; (d) SEM image of $\text{Cu}_2\text{O}@$ HKUST-1 nanowires obtained with a PVP concentration of 1 mg mL^{-1} and an overall reaction time of 30 min; (e) XRD pattern and (f) SEM image of $\text{Cu}_2\text{O}@$ HKUST-1 nanowires obtained using a benzoic acid concentration of 58 mM and an overall reaction time of 30 min.

Figure 2d shows the nanowires obtained after the electrochemical oxidation in the presence of PVP with a lower concentration, i.e. 1 mg mL^{-1} . As expected⁶², and in agreement with the XRD pattern, the MOF nanoparticles at the surface of these Cu_2O nanowires appear larger in size compared to the ones obtained using a higher amount of PVP in the electrolyte. While the size of the nanoparticles obtained using 5 mg mL^{-1} of PVP is in the range of 10–50 nm, the ones obtained using 1 mg mL^{-1} of PVP are overall larger, reaching sizes of more than 100 nm in some cases. This trend is also in agreement with the XRD patterns, since the MOF nanoparticles obtained with a lower concentration of PVP generated sharper reflections, which is also highlighted by the calculated FWHM values. We therefore conclude that the size of the MOF crystals can be tuned by changing the concentration of PVP dissolved in the electrolyte solution and the overall reaction time.

However, one of the drawbacks of using capping agents with a long alkyl chain, such as PVP, is that the capping agent molecules might stay bonded to the surface⁶³. This is a major drawback for some applications, such as catalysis or sensors, where the chemical properties of the nanoparticle's surface play a major role. We therefore explored the possibility of substituting PVP with benzoic acid, which is a well-known modulator in the MOF field⁶⁶. Modulators are typically molecules that are similar to the organic linkers used for the specific MOF synthesis, but bearing only one functional group (i.e. carboxylate in our case). The modulator therefore reacts with the metal oxo-cluster during MOF synthesis but does not lead to the formation of a MOF, since it

lacks the additional carboxylate functional group. Therefore, modulators are useful to slow down the dissolution–recrystallization mechanism, leading in some cases to the formation of single crystalline MOF particles⁶⁷. However, they can also be used to slow down the crystal growth rate⁶⁸. With this intention, we explored the use of benzoic acid instead of PVP, in order to obtain a similar control over the crystal size of the MOF nanoparticles during the electrochemical oxidation, while at the same time keeping the surface of the MOF crystals free of any capping agent.

Figure 2f shows the nanowires that were obtained by performing the conversion reaction in the presence of 58 mM benzoic acid (BA), which corresponds to a BTC:BA molar ratio of 1:10. Also in this case, the nanowires appear covered with MOF nanoparticles, which is also confirmed by the XRD pattern shown in Fig. 2e. Compared with the samples obtained using PVP, the nanowires converted using benzoic acid appear more uniformly covered with MOF nanoparticles. However, in this sample we also noticed the presence of large MOF crystals separated from the nanowires, as shown in Fig. S8, together with the MOF nanoparticles surrounding the Cu₂O nanowires. These larger MOF particles are similar to the case in Fig. S5 where no additives were used. The influence of the concentration of benzoic acid on the morphology of the resulting MOF nanoparticles was also studied and the results are reported in Fig. S9.

In order to rule out the possibility that the nanoparticles shown in Fig. 2b–d,f could originate from a different material than HKUST-1, we performed a series of “control syntheses”, in which the same electrochemical conversion process was performed using an electrolyte with the presence of either PVP or benzoic acid, but with the absence of BTC, which is needed to form the MOF particles. The SEM characterization of these samples is reported in Figure S10 and shows that indeed no nanoparticles are formed at the surface of the Cu₂O nanowires when the synthesis is performed in the absence of BTC in the electrolyte, which further confirms the successful synthesis of Cu₂O@HKUST-1 nanowires.

The Cu₂O and Cu₂O@MOF nanowires were also characterized by transmission electron microscopy (TEM), low-angle annular dark-field scanning transmission electron microscopy (LAADF-STEM) and energy-dispersive X-ray spectroscopy (EDX) (Fig. 3). Figure 3a shows a bright-field (BF) TEM image of the Cu₂O nanowires before their conversion into a MOF and Fig. 3b,c show LAADF-STEM images of Cu₂O nanowires from the same sample. The images highlight the very smooth surface of the nanowires, both at the micrometer and at the nanometer scale. The crystallinity of the nanowires, which was already demonstrated by the XRD pattern presented in Fig. 1g, is confirmed by selected area electron diffraction (SAED) as shown in the inset in Fig. 3a.

Figure 3d shows a LAADF-STEM image of the Cu₂O@MOF nanowires obtained using PVP with a concentration of 5 mg mL⁻¹ and a reaction time of 30 min, while Fig. 3e,f show BF-TEM images of the same sample. In agreement with Fig. 2c, the nanowires appear discontinuously covered by MOF nanoparticles with sizes in the range of 10–50 nm. At high magnification, the interface between the MOF particles and the Cu₂O nanowire appears textured with a fine-grained zone with grain sizes in the range of 10–20 nm (Fig. 3f). These crystalline nanoparticles appear embedded in a light matrix, and most likely result from the incomplete oxidation process of the Cu₂O, with the MOF particles growing around these nanoparticles as soon as the Cu²⁺ ions were available. The MOF particles are clearly visible due to their strong contrast with the Cu₂O nanowires. A close inspection reveals that very small particles (< 5 nm, visible as small dark dots in the regions indicated by the blue circles and enlarged in the inset in Fig. 3f) are embedded within the MOF nanocrystals, which might be small Cu₂O nanoparticles that were not completely converted into MOF. Figure 3g,h show BF-TEM and LAADF-STEM images, and the corresponding EDX line scan across the MOF-Cu₂O interface (orange line in Fig. 3g,h) with the atomic quantification of the different elements present is reported in Fig. 3k. The EDX analysis confirms that the particles surrounding the Cu₂O wires correspond to the MOF, since the amount of C detected quickly drops at the interface, while the signal for Cu increases at the same point. The signal for C drops almost to zero, since a very small amount of C atoms are present in the Cu₂O and the sample substrate, whereas the amount of Cu is approximately 20 at% inside the MOF crystal, corresponding with the presence of Cu in the Cu₃(BTC)₂ nanoparticle. Similar results were obtained in the case of the Cu₂O@HKUST-1 nanowires synthesized using benzoic acid instead of PVP, of which the LAADF-STEM and EDX characterization is reported in Fig. S11.

Additional X-ray photoelectron spectroscopy (XPS) characterization is reported in Fig. S12. The Cu 2p spectra show the presence of Cu⁺ and Cu²⁺ oxidation states (peaks centered at 932 eV and 934 eV, respectively) for all samples, independently on the presence of MOF particles around the Cu₂O nanowires. The presence of Cu²⁺ for the case of pristine Cu₂O nanowires can be attributed to the oxidation of their surface in air⁶⁹.

In summary, we have shown that the electrochemical synthesis of MOFs can be extended to the preparation of hybrid materials where MOF nanoparticles are grown at the surface of metal oxide nanostructures, such as Cu₂O@HKUST-1 nanowire arrays standing on a support. Our synthesis method addresses two major challenges: (i) controlling the growth of MOF nanoparticles, which is achieved through electrochemical synthesis combined with the use of the appropriate additives, and (ii) the integration of MOFs in a nanoscale electrochemical device, which is achieved by the formation of the MOF during electrochemical oxidation of the parent nanostructure. We believe that, through this simple electrochemical method, many more MOFs could be integrated on various nanostructures, and that these hybrid materials could find application in fields such as gas-phase photocatalysis and for photoactive gas sensors, where the photoactivity of the metal oxides could be coupled with the gas absorption properties typical of MOFs. Recent studies in this direction show that HKUST-1 could indeed be used in sensors for the detection of CO₂ or the relative humidity^{70,71}.

Conclusions

Here, we presented the preparation of Cu₂O@HKUST-1 nanowires standing on a conductive support, which opens up the possibility to use such hybrid nanostructures in sensing and gas-phase photocatalysis. These composite nanowires were prepared by coupling two established synthesis strategies: (1) templated electrodeposition

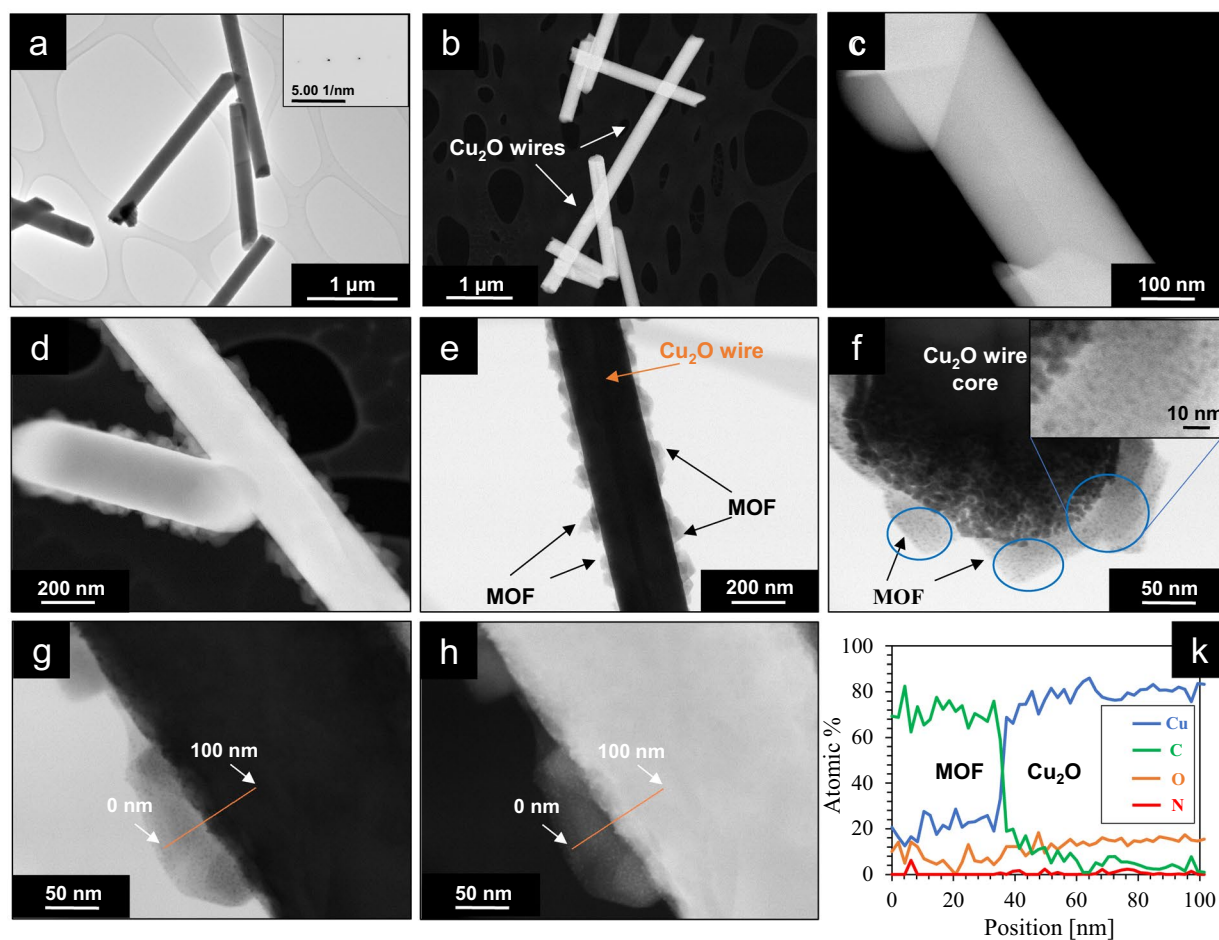


Figure 3. TEM characterization of the $\text{Cu}_2\text{O}@$ HKUST-1 nanowires. (a) BF-TEM and (b) LAADF-STEM images of Cu_2O nanowires before conversion; inset in (a): SAED showing crystallinity; (c) higher magnification image showing the smooth surface of a Cu_2O nanowire; (d) LAADF-STEM image of $\text{Cu}_2\text{O}@$ HKUST-1 nanowires obtained using PVP with a concentration of 5 mg mL^{-1} and a reaction time of 30 min; (e) and (f) BF-TEM images of a $\text{Cu}_2\text{O}@$ HKUST-1 nanowire obtained using the same conditions, with the inset in (f) showing an enlarged area; (g) BF-TEM and (h) LAADF-STEM images of a similar $\text{Cu}_2\text{O}@$ HKUST-1 nanowire at high magnification and (k) corresponding EDX line-scan across the MOF- Cu_2O interface showing an estimation of the amount of C, Cu, N and O (in atomic %) by Cliff-Lorimer quantification.

of Cu_2O nanowires in ion-track membranes with (2) subsequent pulsed electrochemical oxidation of the Cu_2O to obtain HKUST-1 nanocrystals at the surface of the Cu_2O nanowires. Furthermore, we showed that the crystallization of the MOF can be controlled at the nanoscale using PVP as a capping agent, and that the size of the MOF nanocrystals can be tuned by changing the concentration of PVP in the electrolyte. We also showed that the crystallization of the MOF nanocrystals at the surface of the Cu_2O nanowires can also be achieved by using benzoic acid as a modulator instead of PVP. The method allows the integration of MOF nanoparticles on a metal oxide based electrochemical device, and can be potentially extended to other MOFs.

Experimental details. All chemicals used were purchased from commercial sources and used without further purification, namely: sodium hydroxide (NaOH, Carl Roth, $\geq 98\%$), ethanol (EtOH, $\text{CH}_3\text{CH}_2\text{OH}$, Chemsolute, 99.9%), dichloromethane (DCM, CH_2Cl_2 , Chemsolute, 99.9%), copper sulfate pentahydrate ($\text{CuSO}_4 \cdot 5\text{H}_2\text{O}$, Chemsolute, $\geq 99.0\%$), 1,3,5-benzenetricarboxylic acid (BTC, Alfa Aesar, 98%), sulfuric acid (H_2SO_4 , Carl Roth, 95–98%), DL-lactic acid ($\text{C}_3\text{H}_6\text{O}_3$, Fisher Scientific, 90%), polyvinylpyrrolidone K90 (PVP, $(\text{C}_6\text{H}_9\text{NO})_n$, Carl Roth, pure), benzoic acid ($\text{C}_7\text{H}_6\text{O}_2$, Carl Roth, $\geq 99.5\%$), polycarbonate membranes (it4ip, interconnected pores, $0.2 \mu\text{m}$ diameter, pore density: $5 \cdot 10^8 \text{ cm}^{-2}$, $25 \mu\text{m}$ thickness).

Preparation of the Cu_2O nanowires. Polycarbonate membranes were first coated on one side with a 200 nm thick layer of Au and a 500 nm thick layer of Cu using a Leica EM ACE 600 sputter coater. After sputtering, metallic Cu was electrodeposited on the sputtered side of the polycarbonate membrane by adapting a previously published procedure²⁶. In short, an aqueous solution containing 1.0 M CuSO_4 and 0.2 M H_2SO_4 was heated to 60°C , and the Cu was deposited by applying a potential of -0.1 V for 7200 s (2 h) in a two-electrode setup versus a Cu wire that was used as the counter electrode. In the next step, p- Cu_2O nanowires were electrodeposited by

exposing the non-sputtered side of the membrane to the electrolyte, therefore allowing the electrolyte to enter the pores of the membrane. For the electrodeposition, a previously published procedure was used^{45,58,72}. Briefly, an aqueous solution containing 0.4 M CuSO₄ and 3 M lactic acid at pH = 11 was used as the electrolyte, and -0.4 V was applied versus a Cu wire used as the counter electrode in a 2-electrode setup, for a total electrodeposition time of 2000s (~33 min). The pH of the solution was measured with a calibrated pH meter (Accumet AB150pH, Fisher Scientific). Here, the use of a high concentration of lactic acid in the solution is needed to avoid the precipitation of Cu(OH)₂ at a pH of 11. As also reported in ref. 58, the Cu²⁺ ions are stabilized via the formation of copper lactate with the formula Cu(CH₃CHOHCOO)₂. After each electrodeposition, the samples were washed with distilled water, and finally, the polycarbonate membrane was dissolved in DCM.

Partial conversion of Cu₂O into HKUST-1. The obtained Cu₂O nanowires were partially converted into HKUST-1 in the form of nanoparticles that were grown at the surface of the Cu₂O nanowires via a pulsed electrochemical oxidation method. As the electrolyte, a solution containing 5.8 mM BTC in 50/50 (v/v) EtOH/water was used, wherein either PVP or benzoic acid was also dissolved as either a capping agent or a modulator, respectively. In the case of PVP, the concentrations used were 5 and 1 mg mL⁻¹. In the case of benzoic acid, we used 2.9, 5.8, 11.6, 58 and 116 mM and the best results were obtained with a concentration of 58 mM, corresponding to a molar ratio of BTC:benzoic acid of 1:10. Again, a two-electrode setup with a Cu wire as the counter electrode was used, and the electrochemical oxidation was performed using pulsed electrochemistry, during which a pulse of +2.5 V versus Cu for 0.1 s was alternated with a second pulse of 0.0 V versus Cu for 0.5 s, and this was repeated for a total of 100 times, corresponding to a net oxidation time of 10 s at 2.5 V. However, the electrode was immersed inside the electrolyte for a total of either 10 or 30 min, meaning that a resting time of 5 or 15 min, respectively, was applied before and after the electrochemical conversion. All electrodepositions and electrochemical oxidation processes were carried out using an Autolab PGSTAT204 potentiostat (Metrohm).

Characterization. X-ray diffraction (XRD) measurements were performed using a Bruker D2 powder diffractometer equipped with a Cu K α source. SEM images were obtained using a FEI Versa 3D DualBeam. The samples for TEM, LAADF-STEM and EDX characterization were prepared by scraping off the Cu₂O and Cu₂O@MOF nanowires on a Au-mesh covered with an ultrathin C-support film. The characterization was performed using a FEI TEM/STEM TecnaiG2 F20 Super Twin (acceleration voltage: 200 kV; HRTEM resolution: 0.24 nm; STEM-HAADF resolution: 0.19 nm; Thermo-Fisher Scientific/FEI Inc. equipped with an EDAX Si(Li)-detector (EDAX Inc.)). XPS measurements were carried out using a Thermo Scientific K-alpha X-ray photoelectron spectrometer system equipped with a monochromatic Al K α X-ray source. All spectra were calibrated with a reference of C1s (248.8 eV).

Received: 9 May 2023; Accepted: 3 August 2023

Published online: 24 August 2023

References

- Rosi, N. L. *et al.* Hydrogen storage in microporous metal-organic frameworks. *Science* **300**, 1127–1129 (2003).
- Chen, B. *et al.* A microporous metal-organic framework for gas-chromatographic separation of alkanes. *Angew. Chem. Int. Ed.* **45**, 1390–1393 (2006).
- Lu, G. & Hupp, J. T. Metal-organic frameworks as sensors: A ZIF-8 based Fabry-Pérot device as a selective sensor for chemical vapors and gases. *J. Am. Chem. Soc.* **132**, 7832–7833 (2010).
- Wu, M. X. & Yang, Y. W. Metal-organic framework (MOF)-based drug/cargo delivery and cancer therapy. *Adv. Mater.* **29**, 1606134 (2017).
- Nasalevich, M., Van der Veen, M., Kapteijn, F. & Gascon, J. Metal-organic frameworks as heterogeneous photocatalysts: Advantages and challenges. *CrystEngComm* **16**, 4919–4926 (2014).
- Yoon, J. W., Kim, J. H., Kim, C., Jang, H. W. & Lee, J. H. Hybrid photocatalysts: MOF-based hybrids for solar fuel production (Adv. Energy Mater. 27/2021). *Adv. Energy Mater.* **11**, 2170106 (2021).
- Kim, H., Kim, N. & Ryu, J. Porous framework-based hybrid materials for solar-to-chemical energy conversion: From powder photocatalysts to photoelectrodes. *Inorg. Chem. Front.* **8**, 4107–4148 (2021).
- Majewski, M., Noh, H., Islamoglu, T. & Farha, O. NanoMOFs: Little crystallites for substantial applications. *J. Mater. Chem. A* **6**, 7338–7350 (2018).
- Bunzen, H., Grzywa, M., Hambach, M., Spirkl, S. & Volkmer, D. From micro to nano: A toolbox for tuning crystal size and morphology of benzotriazolate-based metal-organic frameworks. *Cryst. Growth Des.* **16**, 3190–3197 (2016).
- Seoane, B., Zamaro, J. M., Tellez, C. & Coronas, J. Sonocrystallization of zeolitic imidazolate frameworks (ZIF-7, ZIF-8, ZIF-11 and ZIF-20). *CrystEngComm* **14**, 3103–3107 (2012).
- Morris, W. *et al.* Role of modulators in controlling the colloidal stability and polydispersity of the UiO-66 metal-organic framework. *ACS Appl. Mater. Interfaces.* **9**, 33413–33418 (2017).
- Zhao, Y. *et al.* Metal-organic framework nanospheres with well-ordered mesopores synthesized in an ionic liquid/CO₂/surfactant system. *Angew. Chem. Int. Ed.* **3**, 636–639 (2011).
- Faustini, M. *et al.* Microfluidic approach toward continuous and ultrafast synthesis of metal-organic framework crystals and heterostructures in confined microdroplets. *J. Am. Chem. Soc.* **135**, 14619–14626 (2013).
- Li, P. *et al.* Synthesis of nanocrystals of Zr-based metal-organic frameworks with csq-net: Significant enhancement in the degradation of a nerve agent simulant. *Chem. Commun.* **51**, 10925–10928 (2015).
- Al-Kutubi, H., Gascon, J., Sudhölter, E. J. & Rassaei, L. Electrosynthesis of metal-organic frameworks: Challenges and opportunities. *ChemElectroChem* **2**, 462–474 (2015).
- Martinez Joaristi, A., Juan-Alcañiz, J., Serra-Crespo, P., Kapteijn, F. & Gascon, J. Electrochemical synthesis of some archetypical Zn²⁺, Cu²⁺, and Al³⁺ metal organic frameworks. *Cryst. Growth Des.* **12**, 3489–3498 (2012).
- Zhang, X. *et al.* Electrochemical deposition of metal-organic framework films and their applications. *J. Mater. Chem. A* **8**, 7569–7587 (2020).

18. Hauser, J. L., Tso, M., Fitchmun, K. & Oliver, S. R. Anodic electrodeposition of several metal organic framework thin films on indium tin oxide glass. *Cryst. Growth Des.* **19**, 2358–2365 (2019).
19. Xiao, Y. *et al.* Oxygen-assisted cathodic deposition of copper-carboxylate metal–organic framework films. *Cryst. Growth Des.* **20**, 3997–4004 (2020).
20. Ameloot, R. *et al.* Patterned film growth of metal–organic frameworks based on galvanic displacement. *Chem. Commun.* **46**, 3735–3737 (2010).
21. Hod, I. *et al.* Directed growth of electroactive metal–organic framework thin films using electrophoretic deposition. *Adv. Mater.* **26**, 6295–6300 (2014).
22. Ameloot, R. *et al.* Patterned growth of metal–organic framework coatings by electrochemical synthesis. *Chem. Mater.* **21**, 2580–2582 (2009).
23. Worrall, S. D. *et al.* Electrochemical deposition of zeolitic imidazolate framework electrode coatings for supercapacitor electrodes. *Electrochim. Acta* **197**, 228–240 (2016).
24. Campagnol, N. *et al.* High pressure, high temperature electrochemical synthesis of metal–organic frameworks: Films of MIL-100 (Fe) and HKUST-1 in different morphologies. *J. Mater. Chem. A* **1**, 5827–5830 (2013).
25. Li, W.-J., Lü, J., Gao, S.-Y., Li, Q.-H. & Cao, R. Electrochemical preparation of metal–organic framework films for fast detection of nitro explosives. *J. Mater. Chem. A* **2**, 19473–19478 (2014).
26. Stassen, I. *et al.* Electrochemical film deposition of the zirconium metal–organic framework UiO-66 and application in a miniaturized sorbent trap. *Chem. Mater.* **27**, 1801–1807 (2015).
27. Schäfer, P., van der Veen, M. A. & Domke, K. F. Unraveling a two-step oxidation mechanism in electrochemical Cu-MOF synthesis. *Chem. Commun.* **52**, 4722–4725 (2016).
28. Caddeo, F. *et al.* Tuning the size and shape of NanoMOFs via templated electrodeposition and subsequent electrochemical oxidation. *ACS Appl. Mater. Interfaces* **11**, 25378–25387 (2019).
29. Stassin, T. *et al.* Vapour-phase deposition of oriented copper dicarboxylate metal–organic framework thin films. *Chem. Commun.* **55**, 10056–10059 (2019).
30. Majano, G. & Pérez-Ramírez, J. Scalable room-temperature conversion of copper (II) hydroxide into HKUST-1 (Cu₃(btc)₂). *Adv. Mater.* **25**, 1052–1057 (2013).
31. Toyao, T. *et al.* Positioning of the HKUST-1 metal–organic framework (Cu₃(BTC)₂) through conversion from insoluble Cu-based precursors. *Inorg. Chem. Front.* **2**, 434–441 (2015).
32. Xu, H., Wang, W. & Zhu, W. Shape evolution and size-controllable synthesis of Cu₂O octahedra and their morphology-dependent photocatalytic properties. *J. Phys. Chem. B* **110**, 13829–13834 (2006).
33. Pan, L. *et al.* Boosting the performance of Cu₂O photocathodes for unassisted solar water splitting devices. *Nat. Catal.* **1**, 412–420 (2018).
34. Poizot, P., Laruelle, S., Grugeon, S., Dupont, L. & Tarascon, J. Nano-sized transition-metal oxides as negative-electrode materials for lithium-ion batteries. *Nature* **407**, 496–499 (2000).
35. Zhang, J., Liu, J., Peng, Q., Wang, X. & Li, Y. Nearly monodisperse Cu₂O and CuO nanospheres: Preparation and applications for sensitive gas sensors. *Chem. Mater.* **18**, 867–871 (2006).
36. Shang, Y. & Guo, L. Facet-controlled synthetic strategy of Cu₂O-based crystals for catalysis and sensing. *Adv. Sci.* **2**, 1500140 (2015).
37. Luo, J. *et al.* Cu₂O nanowire photocathodes for efficient and durable solar water splitting. *Nano Lett.* **16**, 1848–1857 (2016).
38. De Jongh, P., Vanmaekelbergh, D. & Kelly, J. Cu₂O: Electrodeposition and characterization. *Chem. Mater.* **11**, 3512–3517 (1999).
39. Engel, C. J., Polson, T. A., Spado, J. R., Bell, J. M. & Fillingner, A. Photoelectrochemistry of porous p-Cu₂O films. *J. Electrochem. Soc.* **155**, F37 (2008).
40. Movsesyan, L. *et al.* ZnO nanowire networks as photoanode model systems for photoelectrochemical applications. *Nanomaterials* **8**, 693 (2018).
41. Movsesyan, L., Schubert, I., Yeranyan, L., Trautmann, C. & Toimil-Molares, M. E. Influence of electrodeposition parameters on the structure and morphology of ZnO nanowire arrays and networks synthesized in etched ion-track membranes. *Semicond. Sci. Technol.* **31**, 014006 (2015).
42. Molares, M. T. *et al.* Single-crystalline copper nanowires produced by electrochemical deposition in polymeric ion track membranes. *Adv. Mater.* **13**, 62–65 (2001).
43. Toimil-Molares, M. E. Characterization and properties of micro- and nanowires of controlled size, composition, and geometry fabricated by electrodeposition and ion-track technology. *Beilstein J. Nanotechnol.* **3**, 860–883 (2012).
44. Rauber, M. *et al.* Highly-ordered supportless three-dimensional nanowire networks with tunable complexity and interwire connectivity for device integration. *Nano Lett.* **11**, 2304–2310 (2011).
45. Yang, F. *et al.* Cu₂O/TiO₂ nanowire assemblies as photocathodes for solar hydrogen evolution: Influence of diameter, length and NumberDensity of wires. *Z. Phys. Chem.* **234**, 1205–1221 (2020).
46. Huang, G., Yin, D. & Wang, L. A general strategy for coating metal–organic frameworks on diverse components and architectures. *J. Mater. Chem. A* **4**, 15106–15116 (2016).
47. Hu, A. *et al.* Epitaxial growth and integration of insulating metal–organic frameworks in electrochemistry. *J. Am. Chem. Soc.* **141**, 11322–11327 (2019).
48. He, X. & Wang, W.-N. MOF-based ternary nanocomposites for better CO₂ photoreduction: Roles of heterojunctions and coordinatively unsaturated metal sites. *J. Mater. Chem. A* **6**, 932–940 (2018).
49. Zhan, W.-W. *et al.* Semiconductor@ metal–organic framework core–shell heterostructures: A case of ZnO@ ZIF-8 nanorods with selective photoelectrochemical response. *J. Am. Chem. Soc.* **135**, 1926–1933 (2013).
50. Demirel, Ö. H., Rijnaarts, T., de Wit, P., Wood, J. A. & Benes, N. E. Electroforming of a metal–organic framework on porous copper hollow fibers. *J. Mater. Chem. A* **7**, 12616–12626 (2019).
51. Wu, Y. *et al.* Core-shell structured Cu₂O@ HKUST-1 heterojunction photocatalyst with robust stability for highly efficient tetracycline hydrochloride degradation under visible light. *Chem. Eng. J.* **426**, 131255 (2021).
52. Zhan, G., Fan, L., Zhou, S. & Yang, X. Fabrication of integrated Cu₂O@ HKUST-1@ Au nanocatalysts via galvanic replacements toward alcohols oxidation application. *ACS Appl. Mater. Interfaces* **10**, 35234–35243 (2018).
53. Liu, Y. & Tang, Z. Multifunctional nanoparticle@ MOF core–shell nanostructures. *Adv. Mater.* **25**, 5819–5825 (2013).
54. Liu, T. *et al.* Conversion of Cu₂O nanowires into Cu₂O/HKUST-1 core/sheath nanostructures and hierarchical HKUST-1 nanotubes. *RSC Adv.* **6**, 91440–91444 (2016).
55. Ji, H., Hwang, S., Kim, K., Kim, C. & Jeong, N. C. Direct in situ conversion of metals into metal–organic frameworks: A strategy for the rapid growth of MOF films on metal substrates. *ACS Appl. Mater. Interfaces* **8**, 32414–32420 (2016).
56. Ezzati, M., Shahrokhian, S. & Hosseini, H. In situ two-step preparation of 3D NiCo-BTC MOFs on a glassy carbon electrode and a graphitic screen printed electrode as nonenzymatic glucose-sensing platforms. *ACS Sustain. Chem. Eng.* **8**, 14340–14352 (2020).
57. Golden, T. D. *et al.* Electrochemical deposition of copper (I) oxide films. *Chem. Mater.* **8**, 2499–2504 (1996).
58. Maijenburg, A. W. *et al.* Ni and p-Cu₂O nanocubes with a small size distribution by templated electrodeposition and their characterization by photoluminescence measurement. *ACS Appl. Mater. Interfaces* **5**, 10938–10945 (2013).
59. Couderc, J., Garigue, G., Lafourcade, L. & Nguyen, Q. Standard X-ray diffraction powder patterns. *Z. Met.* **50**, 708–716 (1959).
60. Wang, W. *et al.* Hydrothermal synthesis of highly symmetric 26-facet Cu₂O polyhedra. *Cryst. Res. Technol.* **46**, 300–304 (2011).

61. Luo, J. *et al.* Electrochemical conversion of Cu nanowire arrays into metal-organic frameworks HKUST-1. *J. Electrochem. Soc.* **170**, 022506 (2023).
62. Heuer-Jungemann, A. *et al.* The role of ligands in the chemical synthesis and applications of inorganic nanoparticles. *Chem. Rev.* **119**, 4819–4880 (2019).
63. Koczur, K. M., Mourdikoudis, S., Polavarapu, L. & Skrabalak, S. E. Polyvinylpyrrolidone (PVP) in nanoparticle synthesis. *Dalton Trans.* **44**, 17883–17905 (2015).
64. Li, B.-C. *et al.* Size-controlled nanoscale octahedral HKUST-1 as an enhanced catalyst for oxidative conversion of vanillic alcohol: The mediating effect of polyvinylpyrrolidone. *Colloids Surf. A* **631**, 127639 (2021).
65. Yakovenko, A. A., Reibenspies, J. H., Bhuvanesh, N. & Zhou, H.-C. Generation and applications of structure envelopes for porous metal-organic frameworks. *J. Appl. Crystallogr.* **46**, 346–353 (2013).
66. Bao, S., Cai, X., Shi, Y. & Pang, M. Effect of modulators on size and shape-controlled growth of highly uniform In-NDC-MOF particles. *CrystEngComm* **19**, 1875–1878 (2017).
67. Yuan, S. *et al.* A single crystalline porphyrinic titanium metal-organic framework. *Chem. Sci.* **6**, 3926–3930 (2015).
68. Yuan, S. *et al.* [Ti₆Zr₂O₁₂(COO)₁₆] Cluster: An ideal inorganic building unit for photoactive metal-organic frameworks. *ACS Cent. Sci.* **4**, 105–111 (2018).
69. Aria, A. I. *et al.* Time evolution of the wettability of supported graphene under ambient air exposure. *J. Phys. Chem. C* **120**, 2215–2224 (2016).
70. Wang, Q., Lian, M., Zhu, X. & Chen, X. Excellent humidity sensor based on ultrathin HKUST-1 nanosheets. *RSC Adv.* **11**, 192–197 (2021).
71. Hromadka, J., Tokay, B., Correia, R., Morgan, S. P. & Korposh, S. Carbon dioxide measurements using long period grating optical fibre sensor coated with metal organic framework HKUST-1. *Sens. Actuators B Chem.* **255**, 2483–2494 (2018).
72. Maijenburg, A. W., Zoontjes, M. G. & Mul, G. Insight into the origin of the limited activity and stability of p-Cu₂O films in photoelectrochemical proton reduction. *Electrochim. Acta* **245**, 259–267 (2017).

Acknowledgements

We kindly thank Dr. Frank Heyroth for the assistance with the scanning electron microscope. Financial support from the BMBF (Grant No. FKZ:03Z22HN11) is greatly acknowledged.

Author contributions

Conceptualization, F.C., A.W.M.; Formal analysis, F.C.; Funding acquisition, A.W.M.; Investigation, F.C., F.H., B.M., A.M.A.C., D.E., H.Z., T.L., A.H., C.H.; Methodology, F.C., A.M.A.M., A.W.M.; Supervision, A.W.M.; Writing—original draft preparation: F.C.; Writing—review and editing: F.C., B.M., H.Z., A.W.M.; All authors have read and agreed to the published version of the manuscript.

Funding

Open Access funding enabled and organized by Projekt DEAL.

Competing interests

The authors declare no competing interests.

Additional information

Supplementary Information The online version contains supplementary material available at <https://doi.org/10.1038/s41598-023-39982-x>.

Correspondence and requests for materials should be addressed to A.W.M.

Reprints and permissions information is available at www.nature.com/reprints.

Publisher's note Springer Nature remains neutral with regard to jurisdictional claims in published maps and institutional affiliations.



Open Access This article is licensed under a Creative Commons Attribution 4.0 International License, which permits use, sharing, adaptation, distribution and reproduction in any medium or format, as long as you give appropriate credit to the original author(s) and the source, provide a link to the Creative Commons licence, and indicate if changes were made. The images or other third party material in this article are included in the article's Creative Commons licence, unless indicated otherwise in a credit line to the material. If material is not included in the article's Creative Commons licence and your intended use is not permitted by statutory regulation or exceeds the permitted use, you will need to obtain permission directly from the copyright holder. To view a copy of this licence, visit <http://creativecommons.org/licenses/by/4.0/>.

© The Author(s) 2023